ACS APPLIED MATERIALS & INTERFACES

Article

Electrocatalytic (Bio)Nanostructures Based on Polymer-Grafted Platinum Nanoparticles for Analytical Purpose

François Gal, Lylian Challier, Fabrice Cousin, Henri Perez, Vincent Noel, and Geraldine Carrot

ACS Appl. Mater. Interfaces, **Just Accepted Manuscript** • DOI: 10.1021/acsami.6b02956 • Publication Date (Web): 18 May 2016

Just Accepted

ACS Publications

ACS Applied Materials & Interfaces is published by the American Chemical Society.
1155 Sixteenth Street N.W., Washington, DC 20036

Electrocatalytic (Bio)Nanostructures Based on Polymer-*Grafted* Platinum Nanoparticles for Analytical Purpose

François Gal,[§‡] *Lylian Challier,*[φ] *Fabrice Cousin,*[‡] *Henri Perez,*[§] *Vincent Noel*[φ*] *and Geraldine Carrot*[§*]

[§] NIMBE, CEA, CNRS, Université Paris-Saclay, CEA Saclay, 91191 Gif-sur-Yvette Cedex, France.

[‡] LLB, CEA, CNRS, Université Paris-Saclay, CEA Saclay, 91191 Gif-sur-Yvette Cedex, France.

[φ] ITODYS, CNRS, Université Paris Diderot, 15 rue Jean-Antoine de Baïf, 75205 Paris Cedex 13, France.

* Corresponding authors: geraldine.carrot@cea.fr
vincent.noel@univ-paris-diderot.fr

ABSTRACT

Functionalized platinum nanoparticles (PtNPs) possess electrocatalytic properties towards H_2O_2 oxidation, which are of great interest for the construction of electrochemical oxydoreductase-based sensors. In this context, we have showed that polymer-*grafted* PtNPs could efficiently be used as building bricks for electroactive structures. In the present work, we prepared different 2D- nanostructures based on these elementary bricks, followed by the subsequent grafting of enzymes. The aim was to provide well-defined architectures to establish a correlation between their electrocatalytic properties and the arrangement of building bricks. Two different nanostructures have been elaborated *via* the smart combination of *surface initiated*-atom transfer radical polymerization (*SI*-ATRP), functionalized PtNPs (Br-PtNPs) and *Langmuir-Blodgett* (*LB*) technique. The first nanostructure (A) has been elaborated from *LB* films of poly(methacrylic acid)-*grafted* PtNPs (PMAA-PtNPs). The second nanostructure (B) consisted in the elaboration of polymer brushes (PMAA brushes) from Br-PtNPs *LB* films. In both systems, grafting of the glucose oxidase (GOx) has been performed directly to nanostructures, *via* peptide bonding. Structural features of nanostructures have been carefully characterized (compression isotherms, neutron reflectivity and profilometry) and correlated to their electrocatalytic properties towards H_2O_2 oxidation or glucose sensing.

KEYWORDS. platinum nanoparticles, *Langmuir-Blodgett* films, polymer brushes, neutron reflectivity, amperometric biosensor, glucose oxidase.

INTRODUCTION

Amperometric biosensors based on Glucose Oxidase (GOx) are particularly interesting due to their simplicity, reliability and cheapness, leading to their use in commercialized continuous glucose monitoring equipment.[1,2] Any improvement to optimize existing glucose sensor devices or to develop a new one, will find a positive feedback from diagnostic and care health industry.[3,4] The critical point that mainly controls the final glucose monitoring device specification, is its ability to operate at low potential, limiting interferences (vitamin C, lactic acid, etc...). This aspect is classically addressed through the use of molecular, macromolecular and nanomaterial electrocatalysts that decrease the over potential associated to oxidation or reduction of the enzyme product.[5,6]

However, enzymatic electrodes are complex heterogeneous catalytic systems due to the number of involved physico-chemical processes: from the glucose transport towards the enzymatic layer, to the charge transfer reaction of the enzyme product (hydrogen peroxide, H_2O_2). The optimization of such electrocatalytic architectures requires a deep understanding of charges and matter transports at the nanoscale, both having a direct impact on the resulting current intensity per analyte number, *i.e*, on the sensitivity.[7-12] To identify the rate limiting step and the pertinent device optimization way, two main approaches may be considered. Several surface probe microscopies coupled to charge transport/transfer properties measurements, afford a fine correlation between the nanoscale morphology and the local electrocatalytic reaction mechanism and kinetics.[13] While extremely powerful, such methodologies require an important statistical validation, *i.e.*, sampling different structure areas, in order to correlate the local reactivity to the overall electrocatalytic properties of devices. A complementary approach consists in starting from well-defined nano-objects having controlled and tuneable compositions and sizes. Using a bottom-up approach, those

elementary building blocks can be assembled to form nanoscale organized architectures. In such conditions, the overall electrocatalytic mechanism can be easily studied and correlated to the structural unit brick, *i.e.*, to the nano-object.

Due to their high surface area, together with their versatility in shape and composition, metallic nanoparticles have attracted strong attention during the past decade, particularly platinum nanoparticles (PtNPs).[14-17] Indeed, PtNPs show excellent electrocatalytic efficiency towards oxidation and reduction of H_2O_2, the GOx catalytic cycle by-product. Recent advances in nanoparticles' surface functionalization such as *surface initiated*-atom transfer radical polymerization (*SI*-ATRP) from PtNPs, allow the design of polymer-*grafted* PtNPs with tuneable polymer chain length and composition.[18] The advantage of this approach is also the possibility to further insert biomolecules *via* appropriate polymer functional groups,[19] while keeping the Pt core accessible for heterogeneous electron transfer reaction.[20] Indeed, polymer grafting will permit to fill all these requirements (lower grafting density, higher amount of functional groups), and to provide the requisite mobility to facilitate reactions and exchanges.

However, beside requirements concerning nano-object features (individual properties), the way to organize these nano-objects onto a surface (collective behaviour) also has a critical impact on the final electrocatalytic properties. Indeed, the overall current density is controlled by one or several kinetics related to nanostructure features: (i) glucose diffusion rate towards enzyme catalytic centre (oxygen diffusion is assumed to be faster than glucose), (ii) enzyme kinetics, (iii) hydrogen peroxide diffusion rate towards PtNPs, and (iv) charge transport rate from PtNPs to the current collector (conductive substrate).

The aim here is therefore to design and to study well-defined model nanostructures based on polymer-*grafted* PtNPs functionalized with glucose oxidase (GOx), in order to clarify nanoscale phenomena controlling the macroscopic electrochemical signal. Different routes

have been used to construct two different controlled and robust nanostructures from the same building bricks, *i.e.*, polymer-*grafted* PtNPs. The first one (nanostructure A) consisted in the elaboration of *LB* films from PMAA-*grafted* PtNPs (PMAA-PtNPs), obtained from *SI*-ATRP. The second one (nanostructure B) relied in the construction of PMAA brushes with different thickness, *via SI*-ATRP from *LB* films of Br-PtNPs (Scheme 1). GOx was then grafted right after nanostructure assembly. All these architectures have been characterized in details through compression isotherms, neutron reflectivity and other techniques (TEM, profilometry, AFM). Finally, electrochemical studies of nanostructures, towards H_2O_2 and glucose, have been reported to identify the pertinent parameter(s) that have to be taken into account for electrocatalytic nanostructures design.

EXPERIMENTAL SECTION

Materials. Monomer (*ter*-butyl methacrylate) (*t*BuMA, Aldrich) was distilled from calcium hydride prior to use. Glucose oxidase (GOx) from *Aspergillus niger* type XS, 150 000 Units/g from Aldrich, was used directly without any purification procedure. All other reactants were purchased from Aldrich and used as received.

***Surface initiated*-Atom Transfer Radical Polymerization (*SI*-ATRP) of *ter*-butyl methacrylate.** Initiator-derivatized Platinum Nanoparticles (Br-PtNPs) have been prepared according to already published procedures.[18,21] Br-PtNPs (60 mG) in dimethylacetamide (12 mL), $Cu^{I}Br$, and PMDETA were mixed in a three-neck flask under nitrogen. The $Cu^{I}Br$/PMDETA/initiator molar ratio was 2:3:1. The reaction mixture was stirred until it became homogeneous. Then, temperature was increased to 60 °C and the reaction started after addition of the monomer (*t*BuMA). Similar procedure was used for *SI*-ATRP of *n*-butyl methacrylate.[18]

Hydrolysis of *ter*-butyl moieties. 100 mg of poly(*t*BuMA)-*grafted*-platinum nanoparticles (P*t*BuMA-PtNPs) was solubilized in 10 mL chloroform before the addition of 400 µL of trifluoroacetic acid (TFA). The reaction proceeded until complete precipitation of poly(methacrylic acid)-*grafted* platinum nanoparticles (PMAA-PtNPs). Efficiency of the hydrolysis reaction has been evaluated from FTIR, thermogravimetry and ^{1}H NMR and was ≥ 90% (see Supporting Information, *SI*).

Formation of *LB* films. Solution of 1 mg/mL of PMAA-PtNPs (~0.1 mg/mL Pt) was prepared in a mixture of DMAc/chloroform (1/3) just before spreading at the water surface of a home-made *Langmuir-Blodgett* (*LB*) trough filled with Millipore-grade water.[22,23] The

compression isotherms have been recorded at 21°C with a compression speed of 0.3 cm²/s, until the film collapse.

Film transfers have been performed onto solid substrates, either vertically by the *LB* route using behenic acid (amphiphilic molecule), or horizontally (*Langmuir-Schaefer* route) by slowly draining the *LB* trough after *Langmuir* film formation. Depending on target experiments, solid substrates were either silicon wafers or electrodes (glass plates). The surface was previously coated by a gold layer deposited on an anchoring chromium layer (vacuum evaporator). Before transfer, gold-coated wafers have been cleaned with O_3 and were therefore hydrophilic. Surfactant molecules could be eliminated from the mixed film *via* diethyl ether washing (verified by FTIR spectroscopy, see *SI*).

Brush synthesis. Wafers (or electrodes) have been previously covered by 5 layers of Br-PtNPs *LB* films, before being introduced into a glass reactor under inert atmosphere. 662 mg of $Cu^{I}Br$ and 1.92 mL of PMDETA have been mixed in 31.8 mL of acetonitrile under N_2, before being transferred to the reactor. Then, 125 mL of the monomer (*t*BuMA) and 0.226 mL of the initiator (ethyl-*α*-bromoisobutyrate) have been added. The solution in the reactor was heated up to 60°C under N_2. At the end, the reactor was cooled down with ice, and coated wafers (or electrodes) were collected and washed with chloroform to extract the non-grafted chains. The remaining solution in the reactor was solubilized in a chloroform/water mixture, then precipitated in cold methanol and filtered. The obtained free polymer has been analyzed by size-exclusion chromatography (SEC, see *SI*).

Grafting of glucose oxidase (GOx). Samples (wafers or electrodes) were immersed in a solution mixture of NHS (2×10^{-3} mol.L^{-1}) and EDC (10^{-3} mol.L^{-1}) for 2 h under stirring. After being rinsed several times with water, the treated surfaces were transferred to a buffer solution (PBS, pH 7.4) containing GOx (5 mg/mL) at 4°C. The mixture was allowed to react for 12 h

and stored at 4°C. Then, samples were rinsed with PBS solution to eliminate the non-grafted enzymes.

Characterization routine techniques. Organic content ($\%_w$ OC) was determined from thermogravimetric analysis (TGA) performed on a TA Instruments Q50, at a scan rate of 20 °C min^{-1}, up to 800 °C, under air. ^1H NMR spectra of grafted polymer chains in $CDCl_3$, were obtained from a Bruker AC-400 spectrometer. Optical UV absorption measurements were carried out using a Varian Cary 100 UV-Visible spectrophotometer and a quartz cuve with a 2-mm path length. Films' thickness was determined using a Dektak 30ST profilometer with a vertical resolution of 3 nm.

Compression isotherms. Compression isotherms were recorded until the highest pressure (before film collapse): 12 mN/m for Br-PtNPs, 30 mN/m for PMAA-PtNPs and 35 mN/m for P*t*BuMA-PtNPs. In the case of P*n*BuMA, collapse has not been observed due to the high compressibility of the objects.

Surface per object has been calculated using the following equation (1):

$$S_{object} = \frac{S_{film}.M_{NP}}{c_0.V_{sp}.\%_w Pt.N_A} \quad (1)$$

With S_{film}, the surface of the Langmuir film, c_0, the polymer-*grafted* PtNPs concentration in $V_{sp,}$ the volume of the solution spread onto the surface, M_{NP}, the molar mass of the platinum core, $\%_w Pt$, the mass fraction of platinum in the object ($\%_w Pt = 1 - \%_w OC$) and $N_{A,}$ the Avogadro number.

X-ray Diffraction measurements. X-ray measurements have been performed directly onto bulk powders in 0.3 mm glass capillaries. The X-ray source was a rotating anode generator (RU200) equipped with a copper target and operated at 50 kV, 20 mA.

Transmission Electron Microscopy (TEM). TEM images were recorded on monolayers manually deposited onto carbon grids at a *Langmuir* film pressure of 28 mN/m, using a Philips CM12 (120 KeV) transmission electron microscope.

Atomic Force Microscopy (AFM). AFM measurements were performed in the tapping mode with an RTESP5 head at a 1 Hz acquisition frequency. Values of the root-meansquare (rms) roughness were obtained from an average over three pictures taken at different positions on each samples (see *SI*).

Neutron reflectivity. Neutron reflectivity measurements were performed on the time-of-flight reflectometer EROS at LLB (CEA/ Saclay). During the experiment, the entire wavelengths range provided by the neutron source from 3 to 25 Å with a constant $\Delta\lambda/\lambda$ of 0.11, was used. For each sample, three angles (0.93, 1.62 and 3.00) with a $\Delta\theta$ of 0.05 were used to get a q range of 0.07 Å < q < 0.2 Å. The experimental resolution was taken into account in the fitting calculation.

Electrochemical measurements. Electrochemical measurements (chronoamperometry) were performed with an AUTOLAB PGSTAT 100 (Metrohm) apparatus controlled by computer. Data were acquired using GPES 4.9007 software (EcoChemie, The Netherlands). Currents have been recorded at a potential of 0.5 V/ECS, under air and a constant solution stirring.

RESULTS and DISCUSSION

The objective of the present work was to design well-defined electrocatalyic nanostructures dedicated to electrochemical (bio)sensing applications. By varying the assembly of the building bricks (polymer and PtNPs), we aimed to clear up the influence of structuration onto the sensors sensitivity. Different nanostructures have been elaborated (Scheme 1). The first one relied on the assembly (*LB* films) of polymer-*grafted* PtNPs (nanostructure A). The second one consisted in the formation of polymer brushes grafted from PtNPs *LB* films (nanostructure B). Then, enzymes could further be attached to these nanostructures *via* polymer functional groups.

Scheme 1

PMAA-PtNPs *LB* films (nanostructure A). The first route consisted in the preparation of *Langmuir* films directly from poly(methacrylic acid)-*grafted* PtNPs (PMAA-PtNPs), followed by transfer onto solid substrates (Scheme 1A). From compression isotherms, averaged structural information can be extracted, such as the area of a unique nano-object. We first observed that compression isotherms of polymer-*grafted* PtNPs *Langmuir* films are dramatically different from those obtained from small molecule corona (Figure 1).[18] Hydrophobic polymer corona made of poly(*ter*- or *n*-butyl methacrylate) (P*t*BuMA or P*n*BuMA) showed a pseudo-plateau between the low and the high-pressure regime, suggesting a transition in the grafted chains' conformation, between mobile polymer chains and entangled ones. However, although *n*-butyl polymethacrylate-PtNPs films remained stable and could still be compressed, *ter*-butyl polymethacrylate-PtNPs films collapsed right after the plateau. This might be due to the difference in T_g (glass transition temperature) and

hydrophobicity between the two polymethacrylate coronas (*i.e.*, T_g = 293K and 391K for the *n*-butyl and the *ter*-butyl, respectively). These structural differences also impacted the inter-particle distances calculated from the isotherms (Table 1). At the same pressure, the surface per object was lower for the *n*-butyl corona (16.4 nm), than for the *ter*-butyl one (20.2 nm), although both polymer/organic contents ($\%_w$ OC) measured by TGA (see *SI*), and sizes measured by SAXS, were similar (Table 1). Therefore, these results highlight the direct influence of slight modification of the polymer corona onto the 2D-organization of the nano-objects.

Figure 1

P*t*BuMA-PtNPs could further be hydrolysed in homogeneous conditions (see experimental section) to provide hydrophilic poly(methacrylic acid)-*grafted* PtNPs (PMAA-PtNPs). Compression isotherm of PMAA-PtNPs films differed completely from the polymethacrylate ones (Figure 1). Both the surface per object and the film compressibility decreased sharply. These dramatic changes in compression isotherms after hydrolysis of the polymer corona, were certainly due to a strong modification of interactions between the polymer corona and the aqueous phase. Grafted PMAA chains are more hydrophilic therefore promote interactions with the aqueous phase, leading to lower steric interactions between objects in the *Langmuir* film. This likely led to a significant decrease of inter-particle distances and to the disappearance of the plateau in compression isotherms. Note that inter-particle distances calculated from isotherms of PMAA-PtNPs, were closed to ones calculated from powders by SAXS. Moreover, no aggregation has been observed from TEM images (Figure 2).

Table 1

Comparison of PMAA- and Polymethacrylate-PtNPs *Langmuir* films again underlines the ability to finely tune nanocatalyst (PtNPs) distances by tailoring the hydrophobic/hydrophilic balance of polymer coronas. Indeed, one of the main advantages of *SI*-ATRP strategy is the easy control of polymer molecular weights (M_n), allowing to modulate the polymer corona thickness. Regarding polymer conversions (PMAA-PtNPs 1 and 2) in Table 1, a clear correlation between the M_n of polymer chains and the surface per object, was evidenced. According to structural information extracted from compression isotherms, the inter-particle distance can therefore be tuned in a large extent, by varying M_n or the nature of the polymer corona.

Figure 2

Formation of *LB* films. Transfer of *Langmuir* films onto solid substrates allowed the characterization of samples at the nanoscale by several powerful techniques such as neutron reflectivity and TEM. For samples collected at 28 mN/m, TEM images showed clearly the formation of monolayers without aggregated nanoparticles (Figure 2). However, a clear difference in nanoparticles density was observed between P*t*BuMA-PtNPs and PMAA-PtNPs films (Figure 2a and 2c).

Pure PMAA-PtNPs *Langmuir* films collapsed at surface pressures compatible with efficient *LB* transfers. Therefore, addition of an amphiphilic molecule (behenic acid) to the initial solution of PMAA-PtNPs (mixed film) was necessary for an efficient vertical transfer onto solid substrates. Note that behenic acid can easily be eliminated from the resulting *LB* film *via* diethyl ether washing as evidenced by FTIR spectroscopy (see *SI*). However, to probe the influence of the surfactant onto the film structure, PMAA-PtNPs pure *LB* films, (*i.e.*, free of

behenic acid) were also prepared using the *Langmuir-Schaefer* route (see experimental section).

Finally, several samples have been prepared containing from 1 to 3 *LB* film layers. Neutron reflectivity (NR) and profilometry measurements have been carried out to estimate homogeneity, thickness and roughness of *LB* films, in order to correlate the electrocatalytic behaviour to the nanostructure features (Figure 3). Here, *LB* films (mixed or pure films) were transferred onto silicon wafers covered by a chromium sublayer and a gold layer. For the NR fit, we then took into account the presence of a 100 nm-gold layer (with the scattering length density: $\rho = 2.87\times10^{-10}$ cm^{-2}) and a 10 nm-chromium sublayer ($\rho = 4.4\times10^{-10}$ cm^{-2}). Spectra (shifted for clarity) are shown in Figure 3, together with the corresponding fit.

Figure 3, Table 2

Reproducible regular Kiessig fringes at small q (*i.e.*, below 0.01 Å^{-1}) were observed on all NR curves. There were due to the gold layer and their position was related to its thickness (100 nm). On the reverse, features of NR curves were very different in the large-q domain (*i.e.*, above 0.03 Å^{-1}). In this regime, oscillations were mainly due to *LB* films (thickness ≤ 10 nm). To determine the thickness of PMAA-PtNPs *LB* films, the entire curve has been fitted with a density profile including the silicon wafer, the 10 nm-chromium layer, the 100 nm-gold layer, and the PMAA-PtNPs *LB* film layer, with the corresponding adjusting parameters (thickness, scattering length density, roughness). Calculated values from neutron reflectivity are summarized in Table 2.

For pure *LB* films of PMAA-PtNPs, the calculated scattering length density (SLD) was the polymer value ($\rho_{\text{pure films}} = 1.3\times10^{-10}$ cm^{-2}). Indeed, the contribution of PtNPs to the layer SLD was negligible due to their low volume fraction. For mixed films, the value of the layer SLD

was lower, due to the contribution of behenic acid ($\rho_{\text{mixed films}}$ ~ -0.3×10^{-10} cm^{-2}). The thickness of one *LB* film layer was close to the PtNPs diameter (*ca.* 3 nm, see Table 2). This tends to confirm that polymer chains were laterally organized onto the surface. Thickness of three *LB* film layers was almost 3-fold higher than the monolayer one, indicating that the structure was maintained even for multilayers (also evidenced by profilometer measurements, see *SI*). Only the roughness changed from 0.5 and 2 nm while increasing the number of layers. No differences have been observed regarding the nature of the films (pure or mixed), indicating that behenic acid only has a minor impact onto the PtNPs organization inside *LB* film structures.

PMAA brushes onto *LB* films of PtNPs (nanostructure B). As mentioned before, kinetics of heterogeneous charge transfer can be controlled by several processes, including charge transport from the reaction zone to the current collector. In a multilayer nanostructure, charge transport arises from the nanostructure/electrolyte interface to the nanostructure/conductive substrate interface. To identify the electrocatalytic rate limiting step, it is therefore interesting to investigate the nanostructures properties of different assemblies and PtNPs-probes distances, while keeping the same elementary electrocatalyst brick units (PMAA-*grafted* PtNPs). The synthesis strategy to obtain PMAA brushes onto ultra-thin films of PtNPs is summarized in Scheme 1B. It consisted in preparing 5 *LB* films layers of initiating Br-PtNPs, from which *SI*-ATRP of *ter*-butyl methacrylate (*t*BuMA) has been performed, leading to the formation of polymer brushes. Then, polymethacrylate chains were hydrolysed to form PMAA brushes. The next step was the grafting of glucose oxidase (GOx), directly onto polymer brushes (as described later on).

***LB* films of Br-PtNPs.** As shown before (Figure 1), Br-PtNPs showed similar compression isotherms than PMAA-PtNPs, with a continuous decrease of the surface per object while the pressure increased, leading to a rapid film collapse. Again, behenic acid was used to achieve

film transfer at higher pressure (*i.e.*, 28 mN/m), leading to transfer rates close to 100% (see *SI*). Behenic acid was then removed *via* diethyl ether washing. TEM of Br-PtNPs films showed that a monolayer was obtained after transfer (see *SI*). However, because a mixed monolayer was not sufficient to cover the substrate surface, stacking of several layers was performed to ensure a complete coverage of the substrate by PtNPs.[23]

As determined before, the grafting density of initiating molecules (α-bromoisobutyrate) at the surface of PtNPs, is 2.4 initiator/nm^2.[18,19] This was the value taken into account for the brush synthesis. ATRP of *ter*-butyl methacrylate (*t*BuMA) from 2D-surfaces has already been described in the literature.[24] Although we found out that the addition of sacrificial initiator was not necessary for an effective and controlled ATRP directly from functionnalized Br-PtNPs,[18] this was not the case for the brush synthesis. Therefore, ethyl-*α*-bromoisobutyrate (free initiator) was added to the solution (see experimental section). The solvent was acetonitrile because it did not solubilize *LB* films of PtNPs, then preventing any removal of films from the substrate, during the polymerization stage. The presence of free chains in solution allowed to perform a polymerization kinetics study as well as a fine determination of molecular weights (M_n) by SEC (see *SI*). M_n values are usually close to the ones of grafted chains.[24] Polymer conversion was 35% after 35 min reaction, with a good control of the polymerization, as stated by the linear variation of $ln([M_0]/[M])$ as a function of $t^{2/3}$ (see *SI*). M_n obtained from SEC measurements varied from 26800 to 30130 g.mol^{-1} with a polydispersity below 1.3 (Table 3).

Table 3

Features (thickness, roughness) of brush structures have been measured by Atomic Force Microscopy (AFM) and neutron reflectivity. Apart from the qualitative analysis of differences

in surface nanostructures (domains with higher dimensions were detected after polymerization, see *SI*), AFM also permitted a local measurement of the thickness. From surface profiles, the thickness of Br-PtNPs *LB* films (5 layers) was found to be 10 nm. After *t*BuMA brush polymerization, the measured thickness was increased to *ca.* 35 nm.

Neutron reflectivity was performed to give an overall measurement of the thickness. Since the brush thickness was expected to be in the 30 nm range, it was anticipated that the presence of the gold layer would hinder its accurate determination, given that Kiessig fringes associated with both layers would fall in the same range of *q*. To overcome this problem, we performed measurements at the solid-water interface, using an H_2O/D_2O mixture whose scattering length density (SLD) matched the one of gold ($\rho_{H2O/D2O} = \rho_{gold} = 4.5\times10^{-10}$ cm^{-2}).

Figure 4

The obtained NR curves are showed in Figure 4. Note that low-*q* fringes due to the gold layer were almost completely vanished due to contrast matching, compared to previous measurements performed at the air/solid interface for PMAA-PtNPs *LB* films (Figure 3). Therefore, scattering of the gold-coated wafer showed essentially a fringe at rather large *q*, arising from the chromium. It has been fitted using a model consisted of a silicon wafer with a 10.7 nm chromium layer and a 218 nm gold layer, with a roughness of 4 nm. For the *LB* film layer of initiating Br-PtNPs, the reflectivity intensity has increased compared to the bare gold layer. This curve has been fitted using the previous model with an extra layer of 10 nm thickness, a roughness of 4 nm, and a scattering length density of 2.97×10^{-10} cm^{-2}, consistent with the presence of platinum and hydrogenated molecules in mixed *LB* films.

The spectrum corresponding to P*t*MABu-PtNPs brushes clearly showed additional oscillations arising from the polymethacrylate chains, as evidenced in the Rq^4 *vs.* *q* Fresnel

representation (insert in Figure 4). Given the numerous layers involved in the system (*i.e.*, chromium, contrast-match gold layer, Br-PtNPs, polymer brush), it was difficult to obtain an unambiguous fit of the profile, particularly regarding parameters estimation of layer inter-diffusion and roughness. Therefore, we performed calculations in which we considered a homogeneous layer to describe the brush layer that matches the minima of oscillations. This led to an accurate estimate of its thickness and roughness of *ca.* 35 nm and 4 nm, respectively.

Assuming that PtNPs deposits lead to planar layer, brushes thickness (γ) is related to the grafting density (σ) through M_n and d, the density of polymer brushes, *via* equation (2).

$$\sigma = \frac{\gamma \times N_A \times d}{M_n} \quad (2)$$

With a thickness of 35 nm (as determined from both AFM and neutron reflectivity) and a M_n of 30130 g.mol^{-1} (as determined by SEC), the calculated grafting density was therefore 0.7 chains/nm^2. This value was close to the grafting density of polymer chains grown in solution from PtNPs.[18,19] The grafting density of initiating molecules at the PtNPs surface being of 2.4 initiator/nm^2, the initiation efficiency is found to be of *ca.* 30%.

Hydrolysis of brushes. Hydrolysis of P*t*BuMA brushes has been conducted to form the corresponding PMAA brushes required for the subsequent grafting of glucose oxidase (GOx). Unfortunately, the procedure using chloroform such as for polymer-*grafted* PtNPs in solution was not efficient in this case. However, hydrolysis was successful in a water-ethanol mixture, but not fully complete. Indeed, from FTIR spectroscopy, a residual peak at 2980 cm^{-1} (CH_3) could still be detected (see *SI*). The shift of the carbonyl peak is also weaker than for the hydrolysis of polymethacrylate-*grafted* PtNPs in solution. However, samples retained water after immersion, therefore attesting that brushes became hydrophilic. Assuming that the grafting density was the same before and after hydrolysis, we could calculate the new brushes

thickness, *via* equation (2) (Table 3). The thickness of PMAA brushes was determined to be between 16 and 18 nm, in the dry state.

Hybrid structures of GOx. Glucose oxidase (GOx) has been covalently anchored to the PAA moieties (films or brushes), using standard peptide bond formation reagents, *i.e.* EDC and NHS (see Experimental Section).[19] After several washing procedures, grafted GOx activity was quantified from UV spectroscopy (see *SI*). The PMAA-PtNPs *LB* film nanostructure (A) showed an enzymatic activity corresponding to an amount of *ca.* 16 ng of active enzyme, corresponding to 0.10 pmol of active GOx. For the PMAA-PtNPs brush nanostructure (B), the enzymatic activity corresponded to 0.4 pmol of active GOx. Therefore, the amount of active enzymes in nanostructure B (brushes) is 4 times higher than in nanostructure A (*LB* film). This is probably due to a higher mobility of polymer chains in the brush structure, leading to a better access of GOx to the activated ester groups.

Figure 5

Nanostructure sensitivities towards H_2O_2 oxidation. Measurements have been carried out using chronoamperometry at 0.5 V/ECS, under air and constant solution stirring. PMAA-PtNPs *LB* film nanostructure (A) with different number of layers (1 to 15) was first investigated. The (stationary) oxidation current has been measured after each addition of H_2O_2, and plotted versus hydrogen peroxide concentration (Figure 5). The obtained curves revealed two distinct parts depending on the H_2O_2 concentration range. From 10^{-6} to 10^{-3} mol.L^{-1}, linear increases of the current intensity versus H_2O_2 concentration were obtained. From slopes measured in this linear part of curves, the structure sensitivity towards H_2O_2 oxidation could be estimated (Table 4). The other part of curves showed no change in current intensities with further addition of H_2O_2.

Whatever the number of layers, the current variation with H_2O_2 concentration kept the same trend and the sensitivity remained in the range of 0.1mA.L.mol^{-1}. Therefore, the number of layer did not influence the electrochemical response of PMAA-PtNPs *LB* film nanostructure (A). Only the structure with a unique layer of PMAA-PtNPs gave a response slightly lower than the other ones. This was probably due to the PtNPs density onto the electrode (only half of one monolayer was covered by PtNPs after removal of the behenic acid). The 15-layers *LB* film structure also displayed lower current values, probably due to lower charge transport efficiency over the nanostructure thickness. For nanostructures having more than one layer, similar current values have been obtained, indicating that the quantity of PtNPs accessible to H_2O_2 remained identical whatever the number of layers. This suggests that only the nanostructure/solution interface was effectively accessible and electroactive towards the oxidation of H_2O_2. Therefore, in nanostructure A, only the layer in contact with the electrolyte contributed to the electrocatalysis of hydrogen peroxide.

Figure 6, Table 4

The same trend of current variation versus H_2O_2 concentration was obtained for the initiating PtNPs *LB* film (5 layers) and the PMAA-PtNPs brush nanostructure (Figure 6). Brush nanostructure (B) displayed the same sensitivity range than initiating PtNPs *LB* films (*i.e.*, respectively 360 and 315 µA.M^{-1}.cm^{-2}), that is *ca.* 4 times higher than nanostructure A (*ca.* 80 µA.M^{-1}.cm^{-2}). As mentioned before, the use of *LB* technique also permitted a fine control of PtNPs density inside the *Langmuir* film, and thus a precise knowledge of the platinum content in each nanostructure. Therefore, sensitivities could be easily normalized towards the platinum content in one layer (Table 4). Interestingly, the normalized sensitivities were closer

for the two PMAA-PtNPs nanostructures A and B (*LB* film and brushes), and for initial PtNPs *LB* film layers.

However, it has been showed that H_2O_2 oxidation onto bulk platinum is an adsorption-controlled mechanism,[25] whereas onto nanostructured materials, the mechanism is also controlled by mass transport.[20,26] Here, Pt content normalized sensitivities of the PtNPs *LB* structure and the nanostructure A are quite identical (*ca.* 327 and 347 $\mu A.M^{-1}.cm^{-2}.\mu g_{Pt}^{-1}$ respectively). This suggests that mass transport rates are similar in both cases. The high accessibility of H_2O_2 is presumably related to the hydrophilicity of PMAA corona which promoted transport of small molecules towards surface active sites**.** Such an assumption is supported by the slightly lower sensitivity of nanostructure B (*ca.* 285 $\mu A.M^{-1}.cm^{-2}.\mu g_{Pt}^{-1}$), for which the hydrolysis was found to be incomplete, leading to a lower swelling of the polymer chains.

From these results, we showed that in both nanostructures, PtNPs (active sites) remained accessible to H_2O_2, and were also sufficiently close to each other to ensure an efficient charge transport inside the films, from electrocatalytic sites located at the electrolyte/nanostructure interface, to the underlying conductive substrate.[27] Therefore, these nanostructures could further be studied for glucose sensing.

Figure 7

Nanostructure sensitivities towards Glucose. For this study, we used GOx grafted onto nanostructure A (5 layers of PMAA-PtNPs *LB* film), and nanostructure B (PMAA brushes onto 5 layers of PtNPs *LB* film). In the range of studied concentrations, the anodic current was proportional to glucose concentration (Figure 7). The calculated sensitivity was 53 $\mu A.L.mol^{-}$

^{1}.cm^{-2}. For comparison, two reference samples were also studied: nanostructure A without GOx, and nanostructure A with physically adsorbed GOx. For the first one, we could observe that no significant response was registered after addition of glucose. For the second one, the sensitivity was 10 times lower (*i.e.*, 6.1 µA.L.mol^{-1}.cm^{-2}) than for the chemically grafted GOx one.

For PMAA brushes (nanostructure B), the sensitivity (219 ± 70 µA.L.mol^{-1}.cm^{-2}), was 4 times higher than for PMAA-PtNPs *LB* film ones (Figure 7). As mentioned before, the amount of active GOx was 0.1 and 0.4 pM for nanostructures A and B, respectively (see *SI*). Hence, the sensitivity is correlated to the amount of enzyme. However, when sensitivities were normalized towards platinum content, closer values were obtained for both nanostructures A and B: 199 and 230 µA.M^{-1}.cm^{-2}.µg$_{Pt}^{-1}$, respectively. Therefore, this is clear from these results that the main parameter controlling the sensitivity is directly correlated to the step involving heterogeneous transfer reaction of H_2O_2 onto PtNPs.

One major advantage of using glucose as a model system is the large number of research works related to it. In this context, bulk platinum has been widely used as material for the electrochemical detection of glucose. The related sensitivities are reported to be roughly 2 orders of magnitude larger than the values obtained from the nanostructures studied here. However, in the present work, we showed that only the last layer of PtNPs was effectively active. This represented a mass of platinum of about 0.23 g/cm². An estimate of the mass of Pt per cm^2 in bulk Pt (based on an atomic radius of 135 pm and a molar mass of 195 g/mol) gives *ca.* 56 mg/cm² of Pt. Therefore, by comparing sensitivities versus the amount of catalyst, our present nanostructures showed sensitivity 10 times greater than bulk Pt. It is therefore likely that, first, each NPs played the role of independent nanocatalyst and second, the diffusion process was improved.[20] These phenomena are due to the particular nature of H_2O_2 oxidation reaction, which is limited by both electronic transfer and matter diffusion.[28]

Here, the study of well-defined structures indicates that one possibility of sensitivity improvement would be to make the sub-layers of PtNPs accessible, *i.e.* to achieve a 3D porous structure.

CONCLUSION

From well-defined bricks (polymer-*grafted* PtNPs), we succeeded in the design and construction of 2D nanostructures based either on PMAA-PtNPs *LB* films (nanostructure A), or on PMAA brushes grown up from Br-PtNPs *LB* films (nanostructure B). These structures have been fully characterized by neutron reflectivity, profilometry and AFM. GOx enzymes were then covalently grafted to both structures *via* peptide bonding. We found out that the amount of grafted enzymes in nanostructure B (brushes) was 4 times higher than in nanostructure A (*LB* films), due to a better access of the enzyme inside the brush structure. This explained the better sensitivity of this latter structure in the electrochemical study (> 2 times higher). Another reason is related to the higher PtNPs density in the layer from which polymer brushes were grown. Indeed, when sensitivities to glucose detection are normalized towards PtNPs content, similar results were obtained for both nanostructures A and B. Therefore, these results showed the interest for the construction of well-defined model hybrid nanostructures, to improve understanding and optimizing of electrochemical biosensors. This approach led to an excellent control of the nanoparticles content in architectures, permitting to clearly identify the limiting process towards sensitivity, *i.e.*, the heterogeneous electron transfer reaction of H_2O_2 at the PtNPs surface. On the basis of present results, we currently investigate more practical nanostructures, showing sensitivity enhancement, and results will be presented in a forthcoming paper. This approach could also further be used in other fields of applications requiring electronic wiring of enzymes, such as for example, biofuel cell devices.

Supporting Information. TGA, polymerization kinetics, FTIR spectroscopy of polymer-*grafted* PtNPs, compression isotherms and TEM of initial Br-PtNPs, profilometry and AFM measurements of the nanostructures, as well as calibration curves and determination of the grafted enzymes content, are all described in the supporting information.

FIGURE CAPTIONS

Scheme 1. Construction of nanostructures: *LB* films of PMAA-PtNPs (Nanostructure A) and PMAA brushes from *LB* films of functionalized PtNPs (Nanostructure B).

Figure 1. Compression isotherms recorded at 0.3 mm/s and 20°C of PMAA-PtNPs 1 (△), PMAA-PtNPs 2 (○), P*n*BuMA-PtNPs (▲), P*t*BuMA-PtNPs 1 (△), P*t*BuMA-PtNPs 2 (○). Insert: compression isotherm of Br-PtNPs ($\%_w$ OC=14.2%).

Figure 2. TEM micrographs of Langmuir films obtained at 28 mN/m and manually spread onto grids, from P*t*BuMA-PtNPs (a), P*n*BuMA-PtNPs (b) and PMAA-PtNPs (c).

Figure 3. Neutron reflectivity curves of PMAA-PtNPs *LB* films spread onto gold-coated silicon wafer: 1 layer (Ix100, i), 3 layers (Ix10, ii) of the pure films, and 3 layers (Ix10, iii) of the mixed films. Solid lines represent the best fitting of density profiles to each experimental data.

Figure 4. Neutron reflectivity curves obtained at the air-water interface ($\rho_{H2O/D2O}$= 4.4 × 10^{-10} cm^{-2}) of the 200 nm gold-covered wafer (□), the *LB* film of 5 layers of Br-PtNPs (○) and the P*t*MABu brushes (▲). Solid red lines represent the best fitting of density profiles to each experimental data. Insert: Rq^4 *vs* q representation of the P*t*MABu brushes reflectivity curve.

Figure 5. Stationary oxidation current (measured at 0.5 V/ECS) versus H_2O_2 concentration, for the PMAA-PtNPs *LB* films (nanostructure A) composed of 1 (●), 2 (■), 3 (▲), 5 (♦) and 15 (▼) layers.

Figure 6. Stationary oxidation current (measured at 0.5 V/ECS) versus H_2O_2 concentration, for the 5 layers of Br-PtNPs *LB* film (▲) and for PMAA-PtNPs brushes (nanostructure B): brush 1 (■), brush 2 (▲) and brush 3 (●).

Figure 7. Stationary oxidation current (measured at 0.5V/ECS) versus glucose concentration, for nanostructure A (5 *LB* film layers) (■) and for nanostructure B (PMAA-PtNPs brushes) (◆) with covalently bound GOx. Control experiment: nanostructure A without GOx (▲) or with physically absorbed GOx (●).

Table 1. Summary of organic content ($\%_w$ OC), surface per object (S_{object}) and inter-particle distances ($D_{interNP}$) calculated from thermogravimetric (TGA) measurements, SAXS and compression isotherms (CI), at 12 mN/m for Br-PtNPs, 30 mN/m for PMAA-Pt 1 and 2, and 35 mN/m for P*n*BuMA-Pt and P*t*BuMA-Pt 1 and 2.

Structure	**$\%_w$ OC (TGA)**	**S_{object} (CI)** ***(nm²)***	**$D_{interNP}$ (CI)** ***(nm)***	**$D_{interNP}$ (SAXS)** ***(nm)***
Br-PtNPs	20.4	9.2	3.3	3.5
P*t*BuMA-Pt 1	77.1	275.5	17.8	11.5
P*t*BuMA-Pt 2	86.5	353.8	20.2	11.3
P*n*BuMA-Pt	86.3	233.2	16.4	10.1
PMAA-Pt 1	69.1	39.9	6.8	7.6
PMAA-Pt 2	80.7	95.7	10.5	9.4

Table 2. Characteristics of PMAA-PtNPs *LB* films spread onto gold-coated silicon wafer, obtained from neutron reflectivity measurements (SLD: scattering length density).

Structure	**Number of layers**	**SLD** ***($10^{-10}cm^{-2}$)***	**Thickness** ***(nm)***	**Roughness** ***(nm)***
Pure film PMAA-Pt	1	1.3	3.2	0.5
Pure film PMAA-Pt	3	1.3	8.9	2.0
Mixed film PMAA-Pt	3	1.0	8.8	1.7

Table 3. Molecular weight (M_n) and polydispersity index (*PDI*) of free chains obtained after *SI*-ATRP, determined from size-exclusion chromatography (SEC); and polymer brushes thickness calculated from neutron reflectivity, before and after hydrolysis, with a grafting density of 0.7 chain/nm, onto 5 layers of Br-PtNPs.

Structure	**M_n ($g.mol^{-1}$) and *PDI***	**γ before hydrolysis *(nm)***	**γ after hydrolysis *(nm)***
Brush 1	30130 (1.3)	35	18
Brush 2	26800 (1.1)	31	16
Brush 3	29130 (1.1)	34	18

Table 4. Sensitivity towards H_2O_2 and glucose of Br-PtNPs *LB* films, nanostructure A (PMAA-PtNPs *LB* films), and nanostructure B (PMAA-PtNPs brushes), as measured directly and after normalization by the PtNPs content.

Structure	Sensitivity towards H_2O_2 ($\mu A.M^{-1}.cm^{-2}$)	Pt content[c] ($\mu g.cm^{-2}$)	H_2O_2 sensitivity per PtNP ($\mu A.M^{-1}.\mu g^{-1}$)	Sensitivity towards glucose ($\mu A.M^{-1}.cm^{-2}$)	Active [Gox] ($pM.cm^{-2}$)	Glucose sensitivity per PtNP ($\mu A.M^{-1}.\mu g^{-1}$)
Br-PtNPs	360	1.1	327	-	-	-
Nanostructure A (films)	80[a]	0.23	347	53	0.4	230
Nanostructure B (brushes)	315[b]	1.1	286	250	0.1	227

[a,b] sensitivity values were averaged values of *LB* films (A) with 2, 3, 4 and 5 layers,[a] and of brush (B) 1, 2 and 3.[b]
[c] Platinum content was determined from the PtNPs density in one *LB* layer.

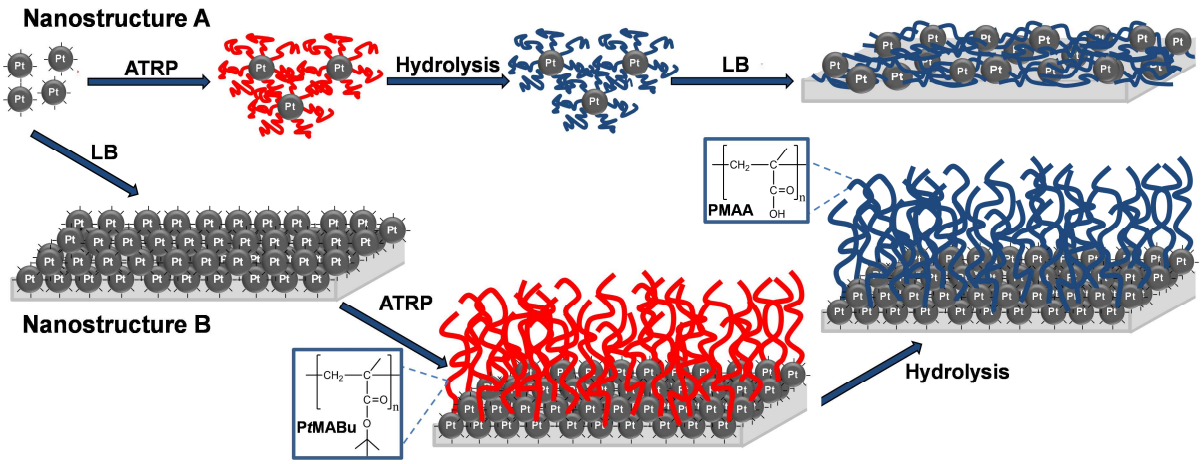
Nanostructure A
ATRP
Hydrolysis
LB
LB
PMAA
Nanostructure B
ATRP
PtMABu
Hydrolysis

Scheme 1

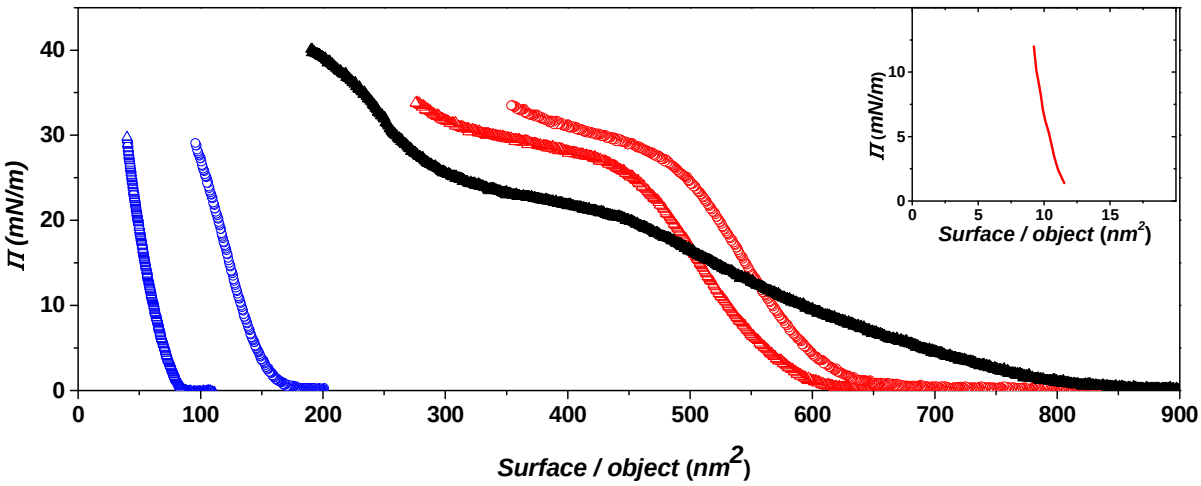
Π (mN/m)
Surface / object (nm²)
0
10
20
30
40
0
100
200
300
400
500
600
700
800
900
Π (mN/m)
Surface / object (nm²)
0
5
10
0
5
10
15

Figure 1

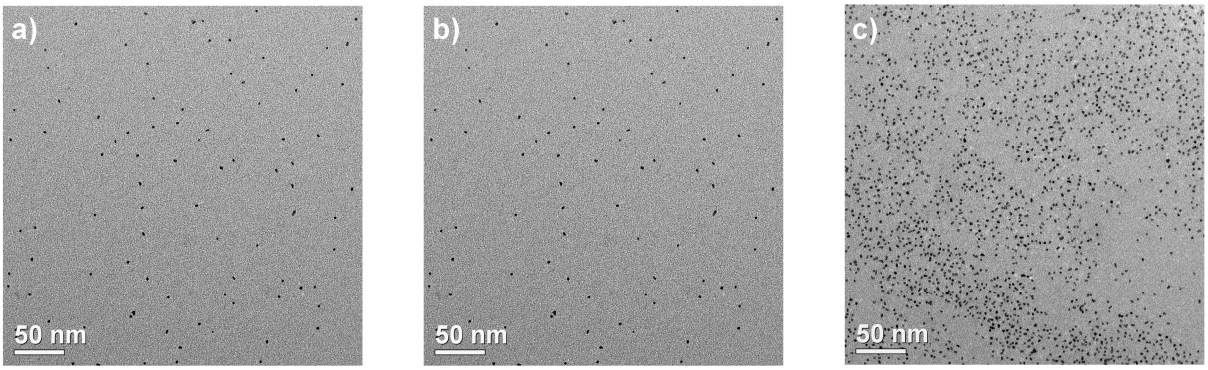

Figure 2

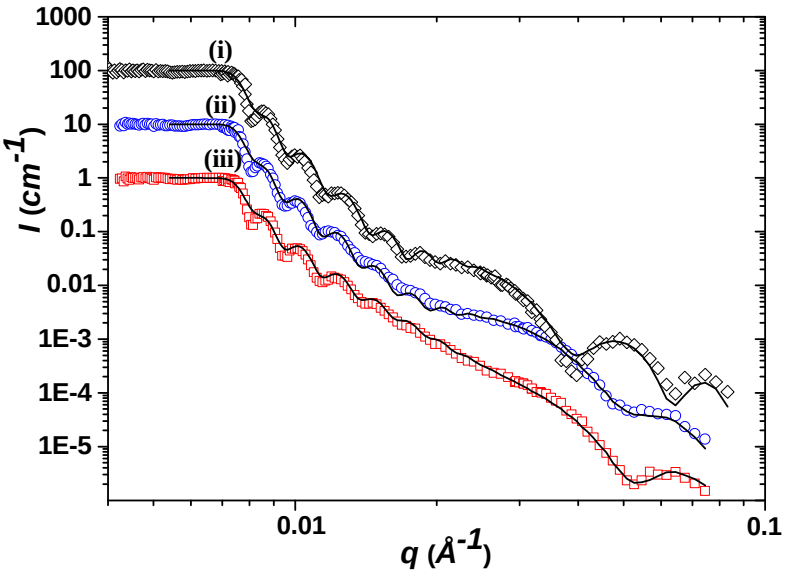

Figure 3

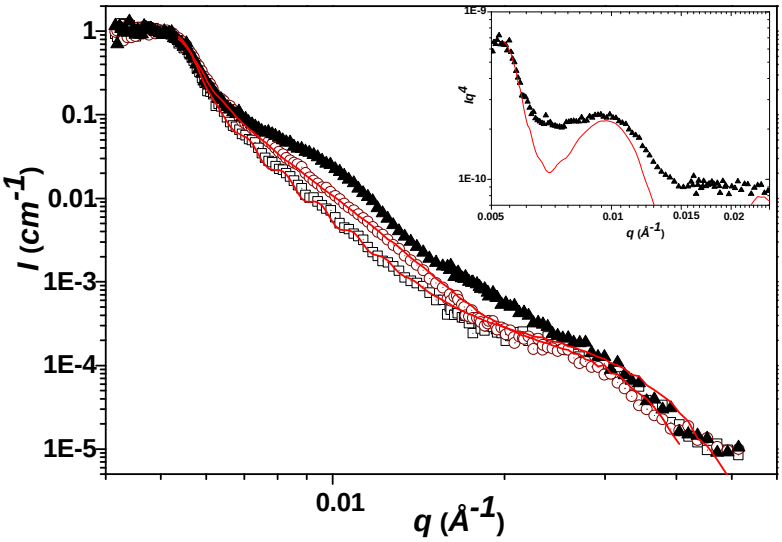
1
0.1
0.01
1E-3
1E-4
1E-5
I (cm-1)
0.01
q (Å-1)
1E-9
Iq4
1E-10
0.005
0.01
0.015
0.02
q (Å-1)

Figure 4

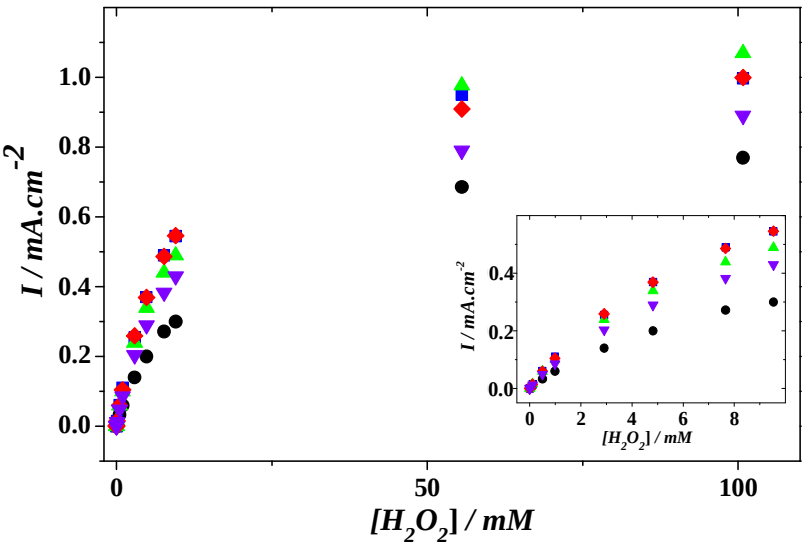
I / mA.cm-2
1.0
0.8
0.6
0.4
0.2
0.0
0
50
100
[H2O2] / mM
I / mA.cm-2
0.4
0.2
0.0
0
2
4
6
8
[H2O2] / mM

Figure 5

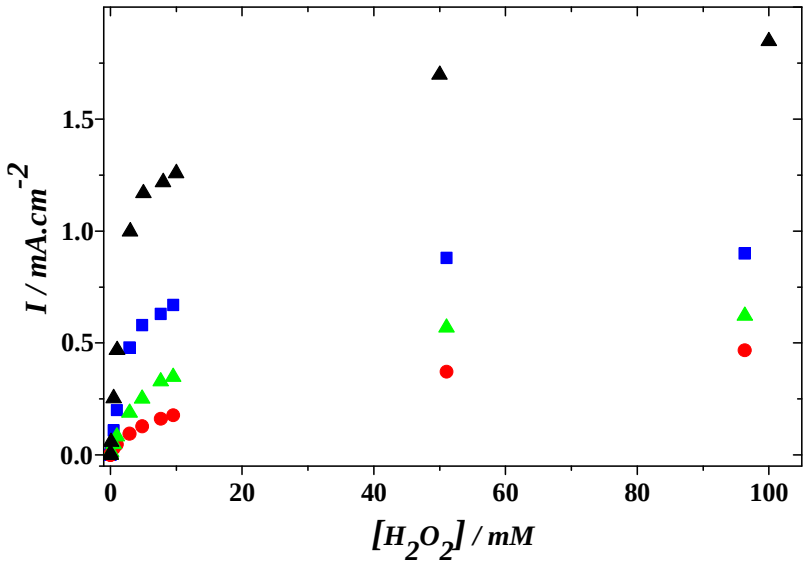

Figure 6

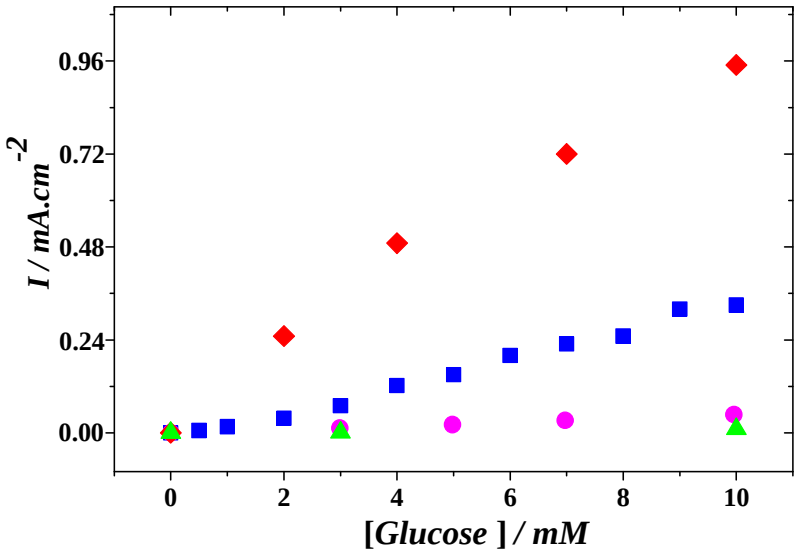

Figure 7

References.

(1) Kerman, K.; Saito, M.; Tamiya, E.; Yamamura, S.; Takamura, Y. Nanomaterial-based Electrochemical Biosensors for Medical Applications. *Trends Anal. Chem.* **2008**, *27*, 585-592.

(2) Wang, J. Electrochemical Glucose Biosensors. *Chem. Rev.* **2008**, *108*, 814-825.

(3) McKeating, K. S.; Aubé, A.; Masson, J.-F. Biosensors and Nanobiosensors for Therapeutic Drug and Response Monitoring. *Analyst* **2016**, *141*, 429-449.

(4) Rice, M. J.; Coursin, D. B. Glucose Meters: Here Today, Gone Tomorrow? *Crit.Care Med.* **2016**, *44*, e97-e100.

(5) Hill, C. M.; Kim, J.; Bard, A. J. Electrochemistry at a Metal Nanoparticle on a Tunneling Film: A Steady-State Model of Current Densities at a Tunneling Ultramicroelectrode. *J. Am. Chem. Soc.* **2015**, *137*, 11321-11326.

(6) Zhu, C.; Yang, G.; Li, H.; Du, D.; Lin, Y. Electrochemical Sensors and Biosensors Based on Nanomaterials and Nanostructures. *Anal. Chem.* **2015**, *87*, 230-249.

(7) Freeman, M. H.; Hall, J. R.; Leopold, M. C. Monolayer-Protected Nanoparticle Doped Xerogels as Functional Components of Amperometric Glucose Biosensors. *Anal. Chem.* **2013**, *85*, 4057-4065.

(8) Palanisamy, S.; Cheemalapati, S.; Chen, S.-M. Amperometric Glucose Biosensor based on Glucose Oxidase Dispersed in Multiwalled Carbon Nanotubes/Graphene Oxide Hybrid Biocomposite. *Mater. Sci. Eng.* **2014**, *34*, 207-213.

(9) Palod, P.; Pandey, S.; Hayase, S.; Singh, V. Template-Assisted Electrochemical Growth of Polypyrrole Nanotubes for Development of High Sensitivity Glucose Biosensor. *Appl. Biochem. Biotechnol.* **2014**, *174*, 1059-1072.

(10) Poulos, N. G.; Hall, J. R.; Leopold, M. C. Functional Layer-By-Layer Design of Xerogel-Based First-Generation Amperometric Glucose Biosensors. *Langmuir* **2015**, *31*, 1547-1555.

(11) Evans, S. A. G.; Elliott, J. M.; Andrews, L. M.; Bartlett, P. N.; Doyle, P. J.; Denuault, G. Detection of Hydrogen Peroxide at Mesoporous Platinum Microelectrodes. *Anal. Chem.* **2002**, *74*, 1322-1326.

(12) Karyakin, A. A.; Puganova, E. A.; Bolshakov, I. A.; Karyakina, E. E. Electrochemical Sensor with Record Performance Characteristics. *Angew. Chem. Int. Ed.* **2007**, *46*, 7678-7680.

(13) Güell, A. G.; Ebejer, N.; Snowden, M. E.; McKelvey, K.; McPherson, J. V.; Unwin, P. R. Quantitative Nanoscale Visualization of Heterogeneous Electron Transfer Rates in 2D Carbon Nanotube Networks. *PNAS* **2012**, *109*, 11487-11492.

(14) Bratlie, K. M.; Lee, H.; Komvopoulos, K.; Yang, P. D.; Somorjai, G. A. Platinum Nanoparticle Shape Effects on Benzene Hydrogenation Selectivity. *Nano Letters* **2007**, *7*, 3097-3101.

(15) Chen, A.; Holt-Hindle, P. Platinum-Based Nanostructured Materials: Synthesis, Properties, and Applications. *Chem. Rev.* **2010**, *110*, 3767-3804.

(16) Tian, N.; Zhou, Z. Y.; Sun, S. G. Platinum Metal Catalysts of High-Index Surfaces: From Single-Crystal Planes to Electrochemically Shape-Controlled Nanoparticles. *J. Phys. Chem. C* **2008**, *112*, 19801-19817.

(17) Tian, N.; Zhou, Z. Y.; Sun, S. G.; Ding, Y.; Wang, Z. L. Synthesis of Tetrahexahedral Platinum Nanocrystals with High-index Facets and High Electro-Oxidation Activity. *Science* **2007**, *316*, 732-735.

(18) Carrot, G.; Gal, F.; Cremona, C.; Vinas, J.; Perez, H. Polymer-Grafted-Platinum Nanoparticles: From Three-Dimensional Small-Angle Neutron Scattering Study to Tunable Two-Dimensional Array Formation. *Langmuir* **2009**, *25*, 471-478.

(19) Gal, F.; Perez, H.; Noel, V.; Carrot, G. Water-Soluble Polymer-Grafted Platinum Nanoparticles for the Subsequent Binding of Enzymes. Synthesis and SANS. *J. Polym. Sci. Pol. Chem.* **2012**, *50*, 289-296.

(20) Challier, L.; Gal, F.; Carrot, G.; Perez, H.; Noel, V. Hybrid Platinum Nanoparticle Ensemble for the Electrocatalytic Oxidation of H_2O_2: Toward Nanostructured Biosensor Design. *Electrochem. Commun.* **2013**, *28*, 118-121.

(21) Perez, H.; Pradeau, J. P.; Albouy, P. A.; Perez-Omil, J. Synthesis and Characterization of Functionalized Platinum Nanoparticles. *Chem. Mater.* **1999**, *11*, 3460-3463.

(22) Perez, H.; de Sousa, R. M. L.; Pradeau, J. P.; Albouy, P. A. Elaboration and Electrical Characterization of Langmuir-Blodgett Films of 4-Mercaptoaniline Functionalized Platinum Nanoparticles. *Chem. Mater.* **2001**, *13*, 1512-1517.

(23) Perez, H.; Noel, V.; Cavaliere-Jaricot, S.; Etcheberry, A.; Albouy, P. A. Nanocomposite Langmuir-Blodgett Films based on Crown Derivatized Platinum Nanoparticles: Synthesis, Characterization, and Electrical Properties. *Thin Solid Films* **2008**, *517*, 755-763.

(24) Sanjuan, S.; Tan, Y. Synthesis of Random Polyampholyte Brushes by Atom Transfer Radical Polymerization. *J. Polym. Sci. Pol. Chem.* **2008**, *46*, 4305-4319.

(25) Hall, S. B.; Khudaish, E. A.; Hart, A. L. Electrochemical Oxidation of Hydrogen Peroxide at Platinum Electrodes. An Adsorption-Controlled Mechanism. *Electrochim. Acta* **1998**, *43*, 579-588.

(26) De Leo, M.; Kuhn, A.; Ugo, P. 3D-Ensembles of Gold Nanowires: Preparation, Characterization and Electroanalytical Peculiarities. *Electroanalysis* **2007**, *19*, 227-236.

(27) Karam, P.; Halaoui, L. I. Sensing of H_2O_2 at Low Surface Density Assemblies of Pt Nanoparticles in Polyelectrolyte. *Anal. Chem.* **2008**, *80*, 5441-5448.

(28) Amatore, C., Savéant, J. M., Tessier, D. Charge transfer at partially blocked surfaces: A model for the case of microscopic active and inactive sites, *J. Electroanal. Chem.* **1983**, *147*, 39-51.

Table of Content/Abstract Graphic (TOC).

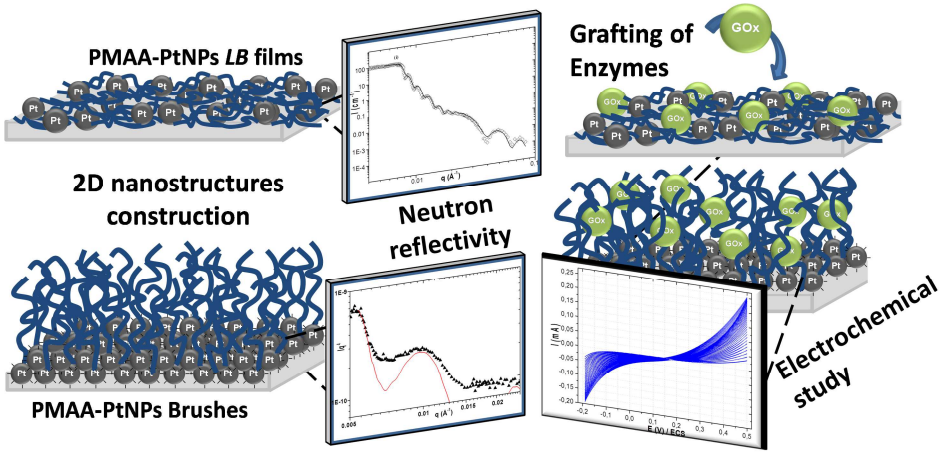

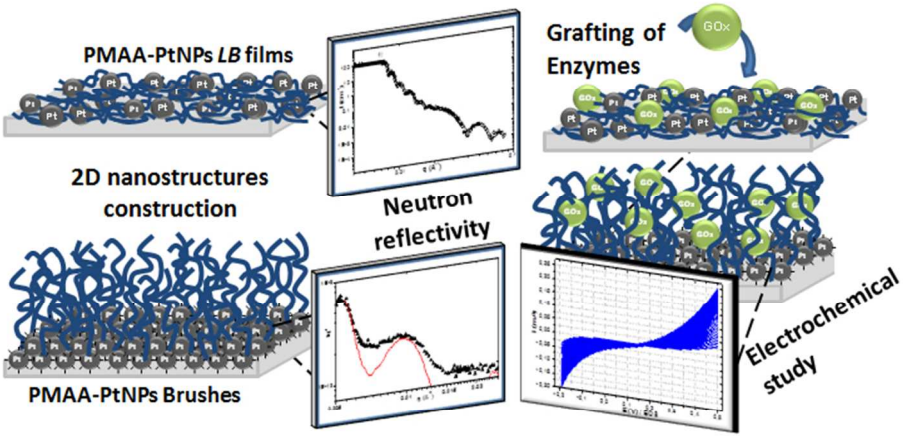

TOC-graphical abstract
211x158mm (96 x 96 DPI)